Materials Science & Engineering A 864 (2023) 144593

Contents lists available at ScienceDirect

Materials Science & Engineering A

journal homepage: www.elsevier.com/locate/msea

The influence of surface finish and build orientation on the low cycle fatigue behaviour of laser powder bed fused stainless steel 316L

William Beard [a,b], Robert Lancaster [a,*], Nicholas Barnard [a], Thomas Jones [b], Jack Adams [b]

[a] Institute of Structural Materials, Bay Campus, Swansea University, Swansea, SA1 8EN, United Kingdom
[b] Rolls-Royce plc., Kings Place, 90 York Way, London, N1 9FX, United Kingdom

ARTICLE INFO

Keywords:
Laser powder bed fusion
Low cycle fatigue
Stainless steel 316L
Surface roughness
Build orientation

ABSTRACT

Additive manufacturing (AM) processes are currently under consideration for marine based components, predominantly due to the numerous benefits that the techniques have to offer over more conventional manufacturing routes. However, there are multiple engineering challenges and questions associated with the introduction of AM based parts into safety critical applications related to the mechanical behaviour of such components. One of the main factors influencing the cyclic performance of a component is the surface finish. As-built AM parts typically exhibit a rough surface owing to partially melted powder being present at the surface and the layer-by-layer nature of the AM process, which together will likely hinder the fatigue response of the component. This behaviour is further influenced by the build orientation of the AM component, with alternative orientations providing a different surface profile alongside a contrasting microstructural morphology. Therefore, alternative finishing methods have been explored to maximise the fatigue performance of components whilst also considering cost and time. This research will explore the low cycle fatigue (LCF) behaviour of laser powder bed fused (LPBF) stainless steel 316L (SS316LN) built in two principal orientations (vertical (90°) and diagonal (45°)) and subsequently subjected to several post-manufacture finishing processes in order to identify the optimal finish for mechanical performance. The mechanical results are supported by microstructural, fractographic and advanced surface profilometry assessments, which have revealed that surface roughness can not be considered alone to be the controlling influence on LCF behaviour. An as-built surface finish will inherently provide a greater number of surface breaking stress raisers, however, a novel mass finishing polishing procedure has been found to produce a similar effective stress concentration factor compared to conventional longitudinal polishing, offering a more viable and less time consuming alternative. Several other key factors must also be considered when assessing the fatigue performance of LPBF built materials, including build direction and the resulting grain orientation, density of the additive structure and the material's sensitivity to the presence of notched features at the surface. Finally, the generated mechanical data has also been interpreted through empirical modelling, and the various data sets have been successfully correlated to enable longer fatigue life predictions.

1. Introduction

Additive manufacturing (AM) is a near net shape manufacturing process currently under consideration by several industrial sectors. The AM process typically builds a three-dimensional part on a layer-by-layer basis, utilising a high energy heat source to selectively melt and fuse two-dimensional slices of a component. The high energy heat source is controlled by digital data from computer aided design (CAD) to build each layer, providing a large element of design freedom for novel geometrical parts without the need for expensive tooling such as punches, dies or casting moulds. This therefore reduces the amount of processing steps, which is not only seen to reduce manufacturing time but also improve component strength and integrity as parts have fewer joining regions removing possible stress raising features [1]. However, one of the main challenges for AM built components is in understanding the variable mechanical response that can typically be produced as a result of the complexities of the process. AM parts typically experience a complex epitaxial thermal history during manufacture, which leads to a degree of build orientation dependency through heterogeneity and anisotropy. Furthermore, AM built materials are also susceptible to

* Corresponding author.
E-mail addresses: 862472@swansea.ac.uk (W. Beard), r.j.lancaster@swansea.ac.uk (R. Lancaster), n.c.barnard@swansea.ac.uk (N. Barnard), thomas.jones2@rolls-royce.com (T. Jones), jack.adams@rolls-royce.com (J. Adams).

https://doi.org/10.1016/j.msea.2023.144593
Received 13 November 2022; Received in revised form 20 December 2022; Accepted 3 January 2023
Available online 5 January 2023

process-induced defects, including lack of fusion (LoF) between subsequent build layers, entrapped gas porosity and an inherently rough surface. Such features all play an important role in defining the mechanical response of the final product, particularly their cyclic properties. Fatigue strength has been found to be more sensitive to microstructural features and defects as compared to more quasi-static deformation mechanisms. As such, AM components can often exhibit inferior cyclic behaviour compared to their traditionally manufactured equivalents, yet offer comparable, or on occasion, superior tensile properties [2–5].

The surface roughness of a sample is defined as the variations in height along the sample surface in relation to the samples' reference plane [6]. Previous studies have found that the as-built surface of an AM sample is considerably rougher and coarser than that of an equivalent specimen finished with a low micron polish. This high surface roughness leads to the formation of surface-breaking stress raising features, which have an adverse effect on the fatigue properties of a given material and can be attributed to partially melted powder particles - the balling phenomenon or the staircase effect [7]. Typically, AM components that are envisaged to be used for high-end applications require an average surface roughness (R_a) of less than 1 μm. This therefore indicates that a high surface roughness, or poor surface finish, is one of the main limiting factors of using AM components within critical applications. Even though it is difficult to remove these features by optimising the parameters of the AM process, they can be reduced or removed by undertaking post-processing treatments such as machining and polishing [8]. It has also been noted in previous studies that even though surface roughness is the main contributor to a reduction in fatigue life within AM components, it cannot be considered alone [9]. Alongside the surface roughness, the presence of internal features such as porosities or areas of LoF must also be considered as these can also have a negative effect [10]. Furthermore, these features have an orientation dependency, where the build orientation can dictate the size and population of such defects.

In this study, the material of focus is the austenitic stainless steel alloy, 316LN (SS316LN), a nitrogen enhanced low carbon derivative of type 316. SS316LN has historically seen extensive use in the marine and nuclear power-plant industry, where the material has been used for components that require a high level of wear and corrosion resistance, sufficient properties across a range of in-service temperatures and be sufficiently weldable. In many of these industrial applications, numerous components exhibit complex and bespoke geometries, thus limiting the use of more traditional fabrication methods. Thus the emergence of additive-based technologies is intimately linked to the increased usage in these industries. Many of these components typically experience a form of cyclic loading during their in-service use, highlighting the need for understanding the fatigue properties of these metallic alloys when manufactured through AM processes. However, the studies on the role of surface finish and build orientation on the fatigue performance of AM SS316LN are relatively limited.

Previously, Zhang et al. [11] investigated how different processing parameters induce the formation of defects in laser powder bed fused (LPBF) SS316LN, and how such features influence the fatigue life of the material when manufactured in the horizontal orientation. They were able to successfully identify the optimal parameters that limited the frequency of defects, and instead, fatigue initiation was found to originate from internal microstructural features. However, specimens manufactured with alternative parameters were found to contain process-induced defects, which acted as sites of stress concentration and crack initiators [11]. Shrestha et al. [12] studied the effect of LPBF build orientation on the low cycle fatigue (LCF) behaviour of SS316L and found that horizontally built specimens offered the best fatigue performance, as compared to the vertical and diagonally built equivalents. In their study, observed fatigue initiation was predominantly sub-surface and attributed to the presence of LoF defects between adjacent melt layers. As such, the condition of the surface finish was not believed to play a major role in the fatigue damage process. Yadollahi et al. [13] assessed the effects of build direction and post-fabrication heat treatment on the fatigue behaviour of LPBF precipitation hardened stainless steel 17-4 and found that the morphology and orientation of porosities resulting from LoF between build layers had a significant effect on fatigue life. They found that the stress concentrations arising from the LoF defects present were considerably higher in the vertically built (90°) orientation compared to those built horizontally (0°), thus leading to a reduction in the fatigue performance [13]. Mower and Long [14] investigated the influence of build orientation, surface roughness and post-build heat treatments on a series of metallic alloy systems fabricated via LPBF, including SS316L. They found that the LPBF SS316L horizontally built material achieved longer fatigue lives than the vertical counterpart, yet LPBF SS316L, irrespective of the build orientation, offered inferior fatigue strength in comparison to the wrought equivalent. Spierings et al. [15] undertook a similar study, investigating the influence of surface roughness on fatigue performance of LPBF SS316L. They found that in the LCF regime, surface roughness had minimal effect on the corresponding fatigue life, however, under high cycle fatigue (HCF) regime conditions where deformation was predominantly elastic, fatigue life was extended when the material was subjected to post-process machining.

In this study, the effects of build orientation and surface roughness on the fully-reversed cyclic performance of LPBF SS316LN is investigated. Extensive surface profilometry data is presented across a range of alternative surface finishes; including as-built, longitudinally polished, circumferentially ground, deliberate R_a machining and a novel mass-finishing procedure. The processes that are most beneficial to fatigue behaviour of LPBF SS316LN are informed using the results of a substantial fatigue programme carried out on laboratory-scale specimens. Fatigue data has been generated for two principal LPBF build directions, vertical (90°) and diagonal (45°), and results collated with surface roughness parameters to establish the best combination of finish and orientation. These results are supported by microstructural and fractographic imagery, in addition to empirical methods in order to understand the sensitivity of LPBF SS316LN to surface discontinuities and determine whether the various data sets can be correlated to enable longer fatigue life predictions.

2. Experimental methods

2.1. Material

The material focussed on in this study is stainless steel 316LN (SS316LN). SS316LN is an austenitic grade of stainless steel with favourable weldability and corrosion resistant properties that is utilised in marine applications. The alloy contains a relatively high concentration of Ni (approximately 12 wt%) and Cr (17 wt%) with a moderate addition of Mo (2.5 wt%).

In this research, gas-atomised SS316LN powder manufactured by LSN Diffusion, with the composition presented in Table 1, was used to

Table 1
Nominal composition of SS316LN powder batch manufactured by gas atomisation.

Element	wt%	Element	wt%
B	0.001	O	540 ppm
C	0.010	O	0.010
Co	0.020	S	0.014
Co + Ta	0.020	Si	0.350
Cr	17.040	Cu	0.010
Fe	Balance	V	<0.010
Mn	1.200	Al	0.005
Mo	2.530	Ti	<0.005
N	0.005	Nb	<0.010
Ni	12.420		

manufacture a series of cylindrical blanks. Prior to fabrication, all powder was sieved to ensure uniformity and analysis of the powder showed a particle size distribution of 5–60 μm, with the full distribution presented in Table 2. The cylindrical rods were fabricated using an EOS M290 machine in an inert nitrogen gas atmosphere.

Standard process conditions defined by EOS for SS316LN were used, with a layer thickness of 20 μm adopted throughout. The value chosen for total energy density (E) is aligned to the study undertaken by Leicht et al. [16], who derived that a total energy density value of between 98.5 and 101.6 J/mm^3 produced the optimal density for LPBF SS316LN parts (99.95–99.99% dense), whilst also offering a favourable build time and not compromising the mechanical properties. Furthermore, Cherry et al. [17] concurred that an optimal energy density of approximately 105 J/mm^3 produced the highest density structures made from LPBF SS316LN. As such, an E value of 100.03 J/mm^3 was used, according to the following equation:

$$E = \frac{P}{v * h * t} \quad (1)$$

Where E = Energy Density (J/mm^3), P = laser power (W), v = laser speed (mm/s), h = hatch spacing (mm) and t = layer thickness (mm).

On the LPBF 45° samples, support structures were required where the sample geometry had a greater than 45° overhang. The supported region was located on the upper radius section, from the gauge length diameter to the maximum sample diameter, and was machined away prior to testing and polishing. No samples failed in this machined surface region that is situated outside of the parallel gauge length and is therefore considered to have negligible effect on the testing results.

2.2. Specimens

Cylindrical rods were built to a height of 125 mm and diameter of 22 mm and were additively-manufactured in two orientations, namely vertical (90°), and diagonal (45°). To investigate the influence of surface roughness, several 90° and 45° aligned specimens were built near net shape with identical parameters and geometries to those previous discussed, but were not subjected to a post process finishing procedure and remained in the as-built condition (Figs. 1 and 2). Following fabrication, all specimens were subjected to hot isostatic pressing (HIP) to further consolidate the material [18]. The HIP cycle consisted of a heat treatment above the SS316LN solution temperature and was held at this temperature for 2–3 h prior to cooling.

In terms of the cylindrical blanks, once they were machined to the specimen geometry, they were subjected to a range of different surface finishes, as follows.

- Circumferentially ground
- Longitudinal Polish – in accordance to ASTM-E606 [19].
- Deliberate machining of R_a = 3.2, producing a circumferentially grooved surface
- Deliberate machining of R_a = 6.4, producing a circumferentially grooved surface
- Machined to ASTM-E606 then polished with mass finishing abrasive media to remove ~150 μm of material
- As-built then polished with mass finishing abrasive media to remove ~150 μm of material

Table 2
Particle size distribution of SS316LN powder.

Cumulative Volume (%)	1	4	25	50	75	90	99
Particle Size Distribution (μm)	≤ 11	12–18	20–26	26–32	34–40	43–49	≤ 60

Fig. 1. LPBF 90° as-built fatigue specimen.

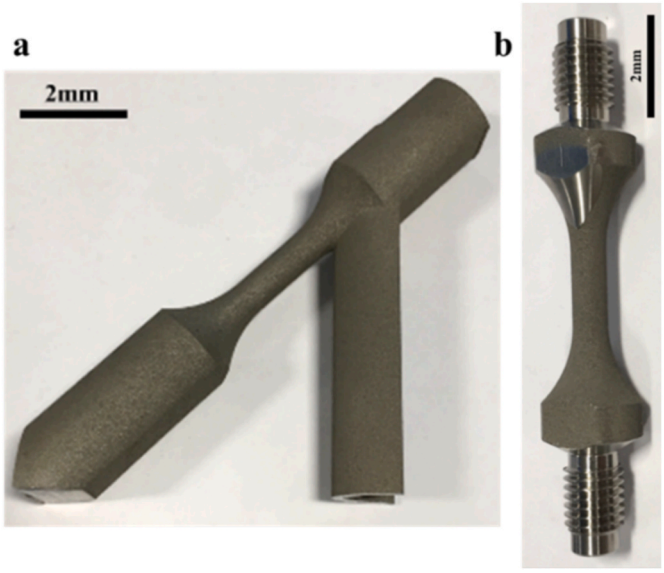

Fig. 2. LPBF 45° as-built fatigue specimen a) with scaffold and b) post-thread manufacture prior to testing.

- As-built then polished with mass finishing abrasive media to remove ~300 μm of material (45° only)

The circumferentially ground and longitudinally polished methods are well established finishing techniques for mechanical test specimens. The test-pieces that were machined and finished to a specific R_a value were deliberately machined via tooling and turned with an excessively high feed rate to generate heavily scalloped surface. In regards to mass finishing, this is seen as a cost and time effective alternative of improving a sample's as-built surface finish. Such techniques have previously found use in the smoothing of pump impellers, blisks for the aerospace industry, high gloss polishing of aluminium car and truck wheels and smoothing and polishing of orthopaedic implants [20].

The mass finishing procedure consisted of subjecting a series of the specimens to ceramic abrasive chip agitated by vibration, in a work bowl flushed with a diluted soap solution to remove waste. This process removes any burrs and rough edges from the manufacturing procedure and can provide an element of surface smoothing and polishing. The quality of the finish is directly dependent on the specific machinery used for the process, the duration of the procedure and the type and grade of abrasive media employed. In this work an AM Solutions M3 system was used to submerge parts in a ceramic media. Specimens were masked in the thread regions to ensure these were not smoothed. In addition, specimens were secured in an additively manufactured fixture connected to the work bowl. This ensured that the ceramic media flowed well and prevented part-on-part contact [20]. The ceramic media used in this study was Rösler abrasive RXX, shape ZS with a size of 04/05 mm. Two regimes of material removal were completed; this included a 150 μm and 300 μm removal on each face.

For comparative purposes, in addition to the LPBF specimens a series of wrought SS316LN specimens with the same composition were also

manufactured, finished with a circumferential polish.

2.3. Low cycle fatigue (LCF) testing

The strain controlled low cycle fatigue (LCF) specimens were machined according to the dimensions depicted in Fig. 3. LCF tests were performed on a servo-hydraulic mechanical test machine according to ASTM E606 [19]) and were tested at 20 °C under controlled laboratory conditions, a 0.004 s^{-1} triangular waveform and a fully reversed R ratio of −1. To provide a range of strain-life data, several applied maximum strain (ε_{MAX}) values were employed, typically 0.18, 0.2, 0.3, 0.6 and 0.8%.

2.4. Surface roughness measurements

Prior to testing, an Alicona Infinite Focus microscope was used to measure the roughness topography and the interrelated parameters of all samples according to ISO 21920–3:2021 [21]. The surface roughness parameters shown in Table 3 were measured to enable a full analysis of the effect of surface roughness on LCF performance. Indicative examples of the surface roughness profiles obtained from the Alicona Infinite Focus microscope are displayed in Fig. 4 for the as-built and longitudinal polished specimens built in the two primary LPBF orientations. Note that the LPBF 45° as-built profile captures the downskin of the specimen.

2.5. Microscopy, defect and fractographic analysis

A Zeiss Smartzoom 5 optical microscope was used to analyse the microstructure and defect population of the different LPBF and wrought SS316LN variants. Specimens were prepared using standard metallograhic procedures, and were then subjected to vibratory polishing on a VibroMet 2 polisher with OP-S (colloidal silica suspension) for ~8 h to remove remaining minor-deformations. Microstructural samples were electrolytically etched with a solution of 10% Oxalic Acid at 3 V and a current of 40–60 mA.

When observing the contrasting microstructures, as was the case in the study by Leicht, attempting to calculate an appropriate average grain size value from such structures is challenging due to the non-uniform nature of the grains and their inherently complexly shaped nature due to thermal gradients during processing, leading to a warped, twisted and bent morphology. Leicht et al. adopted low magnification light microscopy in order to quantify grain size [16]. However, this approach is subject to a level of user error and a resulting average value may be misleading considering the variation in grain size that may be present in a given structure. To overcome such issues, in this study grain detection was performed using the grain area determination in Tango software used, where no border or corner grains were included and boundaries with a misorientation >10 ° were used for measurements of grain size. Grain size of the X–Y and X-Z face of each LPBF variant was measured by the elliptical fit method, excluding any twin boundaries in the grain size calculations. Given the more homogenous nature of the wrought material, only a single face was analysed for grain size and aspect ratio. Using this more automated approach, the resulting grain data is displayed in Table 4.

A Hitachi SU3500 SEM, with electron backscatter diffraction (EBSD) capability, was used to inspect the fracture surfaces. For the fractographic investigations, the tested specimens were sectioned and cleaned ultrasonically in acetone and imaged using an accelerating voltage of 20 kV and working distance of 20 mm. For EBSD analysis, scans were acquired using a step size of 1.5 μm and 4 × 4 binning. The phases chosen for acquisition were FCC-Fe and BCC-Fe, with the band detection mode optimised for EBSD. EBSD data was acquired using the Tango plug-in included in the Channel 5 software.

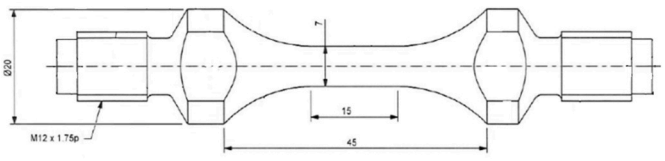

Fig. 3. Specimen geometry for LCF testing.

Table 3
Roughness and surface texture parameters.

Roughness Parameters	
R_a (μm)	Average roughness of profile
R_q (μm)	Root-Mean-Square roughness of profile
R_t (μm)	Total height of roughness profile
R_z (μm)	Mean peak to valley height of roughness profile
R_{MAX} (μm)	Maximum roughness depth
R_p (μm)	Maximum profile peak height
R_v (μm)	Maximum depth of the profile below the mean line within the sampling length
R_c (μm)	Mean height of profile elements
R_{sm} (μm)	Mean spacing of profile irregularities of roughness profile
R_{ku}(μm)	Peakedness of the amplitude density curve
R_{dq} (μm)	Root-Mean-Square slope of roughness profile
R_k (μm)	Core roughness depth
R_{pk} (μm)	Highest profile peak height
R_{vk} (μm)	Deepest profile valley depth
R_{mr1} (%)	Peak material component, the fraction of the surface which consists of peaks above the core material
R_{mr2} (%)	Peak material component, the fraction of the surface which will carry the load
Surface Texture Parameters	
S_a (μm)	Average height of selected area
S_q (μm)	Root-Mean-Square height of selected area
S_p (μm)	Maximum peak height
S_v (μm)	Absolute value of the height of the largest pit within the defined area
S_z (μm)	Maximum height of selected area
S_k (μm)	Core roughness depth, Height of the core material
S_{pk} (μm)	Reduced peak height, mean height of the peaks above the core material
S_{vk} (μm)	Valley depth below the core roughness
S_{mr1} (%)	Peak material component, the fraction of the surface which consists of peaks above the core material
S_{mr2} (%)	Peak material component, the fraction of the surface which will carry the load

3. Results & discussion

3.1. Microstructural analysis

Fig. 5 presents the EBSD inverse pole figure (IPF) maps for the 45 ° and 90° LPBF variants in both the XY and XZ orientations, in comparison to the wrought equivalent. For each LPBF variant, the XZ plane captures the epitaxial build orientation resulting from the LPBF process. Overall, both the wrought and LPBF materials show a predominantly austenitic Face Centre Cubic (FCC) microstructure with minute amounts of retained Body Centre Cubic (BCC) δ-ferrite distributed throughout. Grain measurements, kernel average misorientation (KAM), quantity of Σ3 boundaries (twinning boundaries) and amount of BCC ferrite phase for the wrought and LPBF materials are displayed in Table 4. For the LPBF materials, there is no evidence of a cellular structure inside the grains nor any melt pool boundaries, due to the post manufacture HIP treatment at a temperature above the SS316LN solution temperature. However, as evidenced in Fig. 5b and c, there is still a small presence of high angle grain boundaries (the majority of which can be observed between 30 and 60°), remaining in the respective structures and misorientation is still present inside the larger grains, which suggests that recrystallisation has not occurred.

As given in Fig. 5a, wrought SS316LN exhibits a predominantly equiaxed microstructure in the two alternative orientations, which

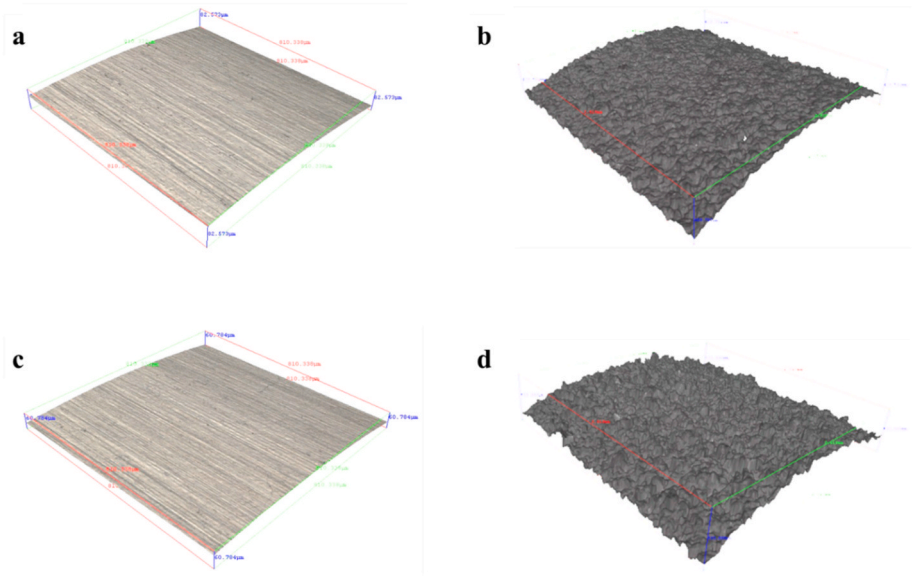

Fig. 4. Alicona surface roughness profiles for a) LPBF 90° longitudinal polish, b) LPBF 90° as-built, c) LPBF 45° longitudinal polish and d) LPBF 45° as-built (downskin) surfaces.

Table 4
Average grain size measurements for SS316LN variants including aspect ratio, average local misorientation, Σ3 length proportion and amount of BCC phase present.

Sample	Average Grain Size (μm^2)	Number of Grains	Aspect Ratio	Average KAM (°)	Σ3 (%)	Amount of BCC phase (%)
Wrought	1061	405	0.821	0.15	49.0	1.5
LPBF 90° XZ	597	542	0.690	0.65	0.57	0.2
LPBF 90° XY	409	1141	0.997	0.55	0.53	0.4
LPBF 45° XZ	609	649	0.846	0.62	0.54	0.5
LPBF 45° XY	488	890	0.660	0.68	0.57	0.2

would typically promote an isotropic response when subjected to loading. This variant also offers the largest comparable average grain size, with grain areas in the order of 1060 μm^2. It also contains the highest percentage of BCC ferrite. In comparison, the 90° LBPF variant (Fig. 5b) exhibits a strongly anisotropic structure as the XZ face shows an elongated microstructure due to epitaxial grain growth along the build direction, with an average grain size of 597 μm^2, whilst an equiaxed grain morphology perpendicular to the build orientation is observed in the XY plane (average grain size of 409 μm^2). As previously reported, this columnar epitaxial grain growth has arisen due to the complex thermal history occurring in the LPBF process [22]. Since LPBF is a layer by layer manufacturing process, a single layer of metal is cast upon a previous single layer. This causes time dependant temperature profiles and often results in an alloy experiencing repeated solid state and liquid solid phase transformations [22]. Additionally, LPBF is a relatively rapid solidification process with reported cooling rates of 10^4 K/s and heat flow in the build direction frequently results in columnar microstructures [22]. In addition to the elongated morphology of the grains on the X-Z face, the 90° material is also characterised by a strong <101> texture parallel to the build direction, with few smaller grains with different crystallographic orientations found in surrounding grain boundary locations. The strong <101> texture is usually formed when the heat flow from the manufacturing process is aligned with the build direction and a strong, uniform thermal gradient can be maintained. This is consistent with the study by Leicht et al. [16] who found a heavily textured <101> structure on the parallel plane to the build direction and stated that the preferential orientation of grains is more aligned to the total energy density rather than specific values of scan speed or hatch spacing.

When considering the presence of twinning in the different variants, there is significant evidence of annealing induced twinning (Σ3 = 49%) in the wrought material, whereas there is little existence of such features in the LPBF equivalents (LPBF 90° = 0.53–0.57% and LPBF 45° = 0.54–0.57%). However, it is important to note that under deformation, twinning induced plasticity (TWIP) becomes more prominent in LPBF materials, particularly structures exhibiting a strong <101> texture [23, 24].

As given in Fig. 5c, the 45 ° LPBF material exhibits an anisotropic structure with elongated grain morphology due to epitaxial grain growth along the build direction (609 μm^2). However, in contrast to the 90° material, the angled build also displays a relatively similar morphology on the orthogonal X–Y face (average grain size of 488 μm^2) due to the titled nature of the layering process, as evidenced by the values stated in Table 4. It is important to note that all LPBF material has been HIPped within the temperature range needed to solution heat treat SS316LN. However, during the HIP cycle it is likely that only partial recrystallisation has occurred as a lower heat solution temperature has been used in comparison to previous studies [25,26] and therefore little microstructural transformation has taken place. Yet, the significant local deformation and temperature range has been successful in closing up any small porosity sites to produce a fully dense structure throughout, reflecting the findings of Leicht et al. [16].

3.2. Low cycle fatigue (LCF) results

The results from the low cycle fatigue (LCF) tests on LPBF SS316LN are presented in Figs. 6–9. Figs. 6 and 7 show the relationship between fatigue life and maximum strain and stress amplitude for vertically and diagonally built specimens respectively, with corresponding strain-stress loop behaviour displayed for monotonic and stabilised conditions for each of the build orientations in Figs. 8 and 9. From Figs. 6a and 7a, the influence of surface finish on fatigue resistance can be seen, and for both the 90° and 45° specimens, the most optimal finishes are shown to be the longitudinal polish and mass finishing procedures. Interestingly, in the mass finished specimens, it appears that the condition of the

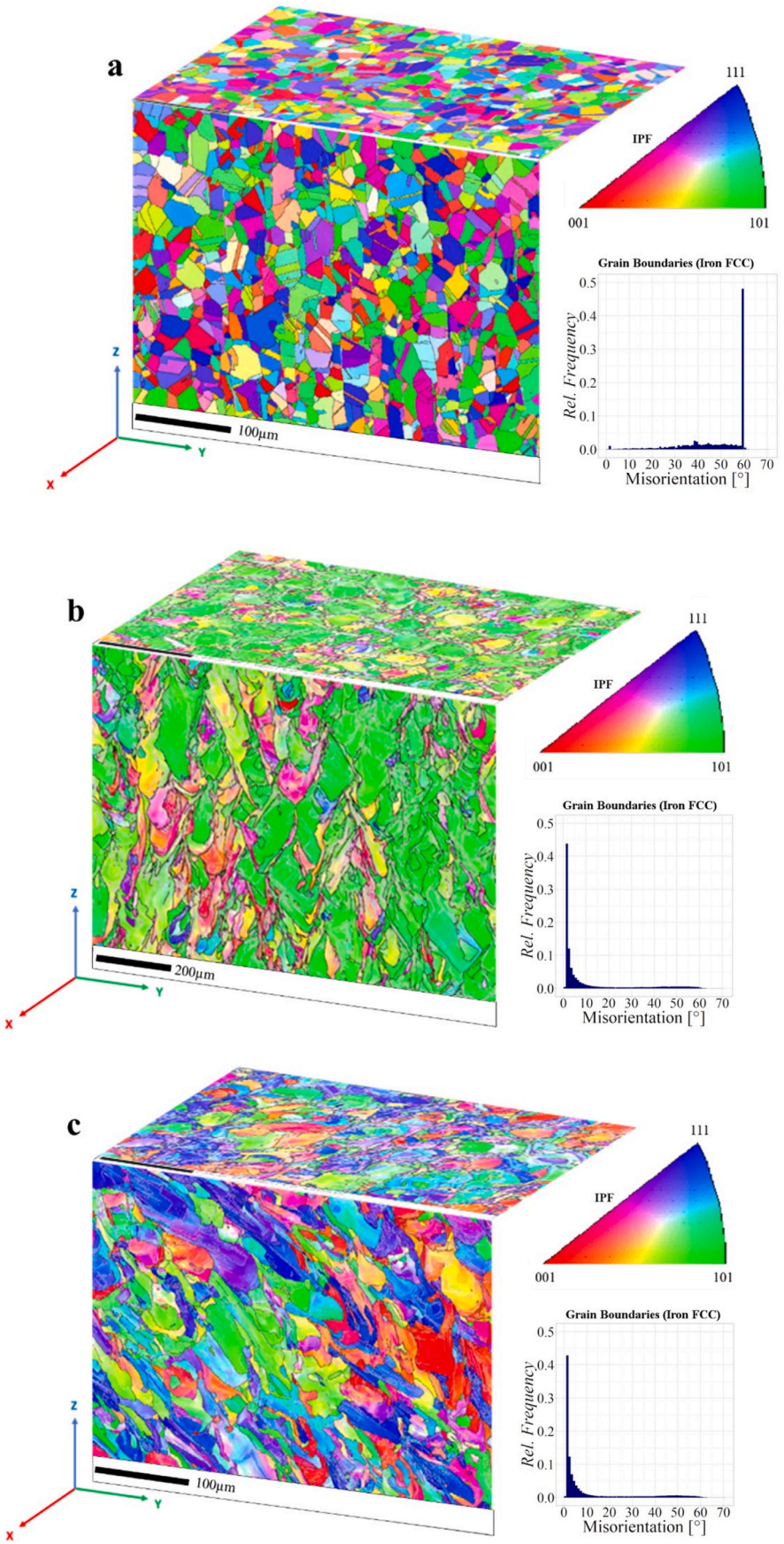

Fig. 5. EBSD Microstructures of SS316LN: a) wrought, b) LPBF 90°, and c) LPBF 45°.

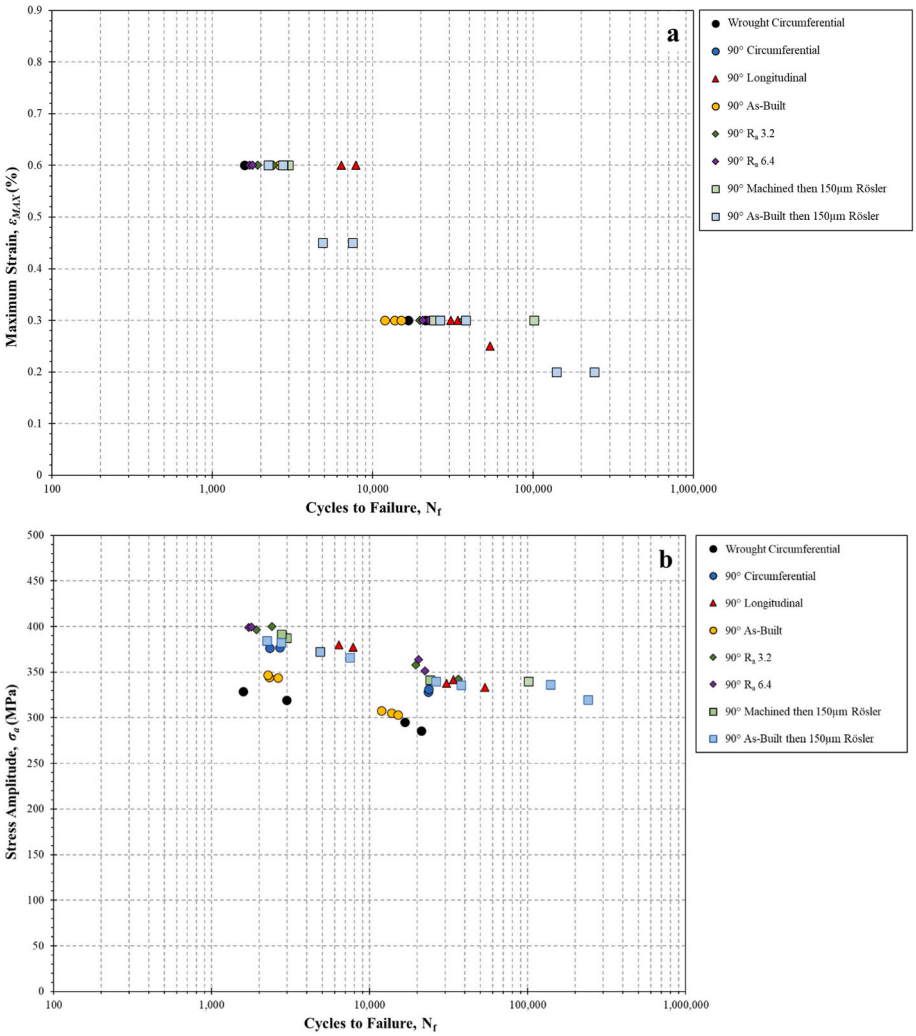

Fig. 6. LCF results for LPBF SS316LN 90° specimens a) ε_{MAX}-N_f and b) σ_a-N_f compared to wrought equivalent.

surface prior to the Rösler procedure does not seem to influence the final fatigue properties of corresponding specimens. This is the case for both LPBF build orientations that were subjected to the 150 µm abrasive media where no discernible difference can be seen in fatigue life that can not be attributed to typical experimental scatter. However, a further improvement in fatigue life is observed when additional surface material is removed in the 300 µm finishing procedure. As given in Fig. 7a, the 300 µm Rösler polish can be seen to extend the fatigue life in the LPBF 45° specimens, providing a resistance to cyclic loading of a similar level to that obtained using the established longitudinal polishing method.

The corresponding stress amplitude behaviour of the same LCF tests on the LPBF materials is given in Figs. 6b and 7b. These figures have further diverged the contrasting data sets and have helped to more clearly establish the knock-down in fatigue life when the surface finish remains in the as-built condition. In both cases, the datapoints for the as-built specimens sit below the majority of the other surface finish types, with most of the other surface finishes offering a tight scatter band. Yet, despite the differences in fatigue life across the LPBF specimens, both orientations exhibit a vastly superior LCF performance as compared to the wrought material in the circumferentially ground state, irrespective of the surface finish applied to them. Previous studies [27] have found that a highly heterogeneous microstructure, like that seen in a LPBF material, can induce a high back stress when cyclically deformed, which in turn acts to inhibit the movement of dislocations. Back stress is associated with the presence of geometrically necessary dislocations (GND), where GND gliding in the softer regions of the microstructure, for instance the <001> orientated grains, will be accumulated at the elastic/plastic domain boundaries leading to the pile up of GNDs at the boundaries producing long range internal stress. In other words, the back stress in the softer grains makes these regions stronger and, simultaneously, the stress concentration near the piling up of GNDs exerts a stronger forward stress in the adjacent harder regions (i.e. the <101> oriented grains). This phenomenon was also found to raise the level of strain hardening in the material [27]. In the present study, the 90° orientated build consists of a heavily textured <101> grain structure, and smaller sized <001> orientated grains, offering a partially bimodal microstructure. The density of GNDs was estimated from the EBSD data given in Fig. 5 using Channel 5 software and it was found that the density of GNDs was distributed unimodally in LPBF 90° and LPBF 45° around approximate values of $0.95 \times 10^{14}/m^2$ and $0.85 \times 10^{14}/m^2$, respectively. In contrast, the modal value for the GND density distribution in the wrought material was found to be approximately $0.15 \times 10^{14}/m^2$ with an upper limit of $0.4 \times 10^{14}/m^2$ observed; considering only the austenitic FCC phase present. Therefore, a considerable back stress is considered to be generated in the 90° LPBF material when subjected to fatigue deformation, which thereby acts to relieve strain localisation and enhance the cyclic loading capability of the material. Furthermore, as given later in Fig. 8a, the 90° build orientation can also be seen to strain harden the most of the three SS316LN variants, owing to the previously described behaviour.

When directly comparing the fatigue properties of 90° and 45° specimens for any given surface finish, the 90° specimens generally offer

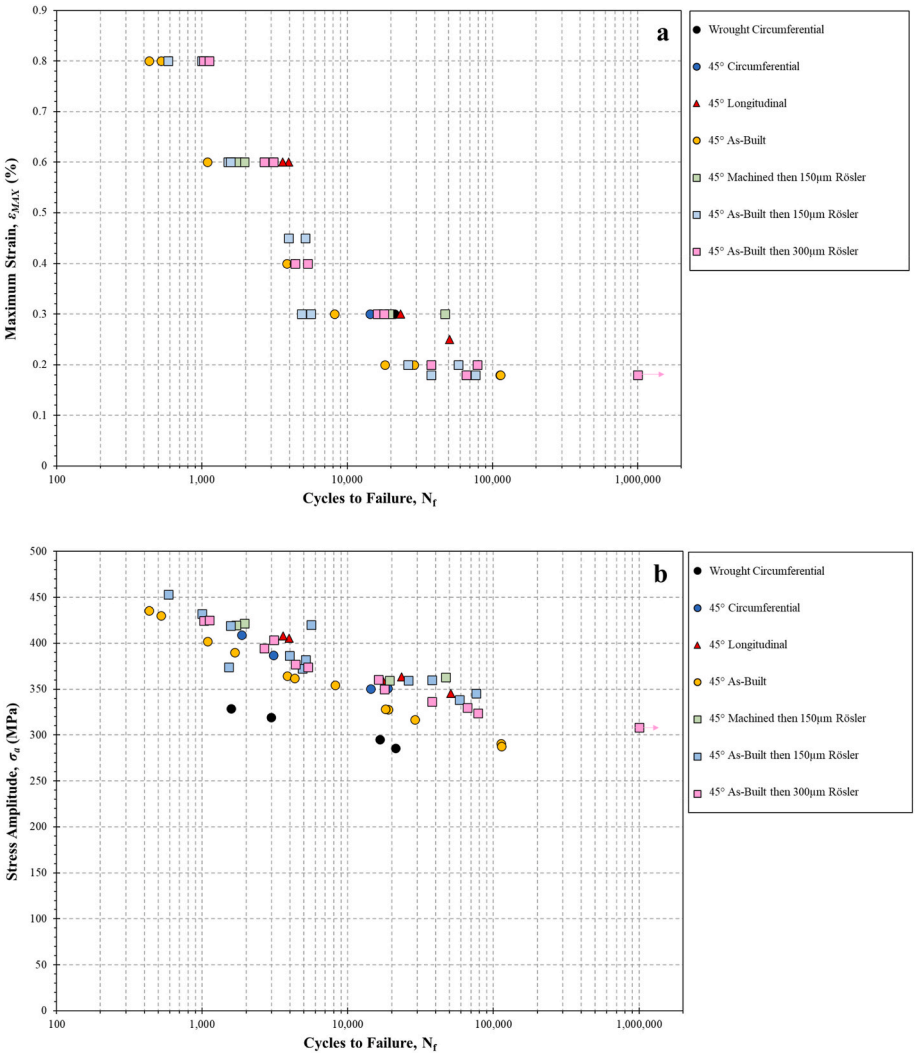

Fig. 7. LCF results for LPBF SS316LN 45° specimens a) ε_{MAX}-N_f and b) σ_a-N_f compared to wrought equivalent.

longer fatigue life. This can be seen in Table 5, where the average fatigue life for specimens tested at $\varepsilon_{MAX} = 0.6\%$ is directly compared and the 90° specimens are more resistant to fatigue throughout. This difference is related to the material's underlying microstructure, which is markedly different due to the nature of the LPBF manufacturing process. As shown in Fig. 4, there is a stronger presence of a columnar structure in the X-Z plane of the 90° build running parallel to the build direction, producing an average grain size of 597 µm^2. However, this is offset by a more equiaxed grain morphology with an increased aspect ratio (0.997 compared to 0.690) on the orthogonal X–Y plane, perpendicular the build and loading directions respectively. On the contrary, in the 45° angled specimens, the average grain size and aspect ratios on the two alternative planes are more similar, due to the nature of the diagonal building process in relation to the representative X–Y and X-Z planes (average grain sizes of 488 µm^2 and 609 µm^2, aspect ratios of 0.660 and 0.846). Given that the maximum resolved shear stress is at 45° to the loading direction and the 90° specimens have a smaller grain size aligned in this plane, this enables a greater volume of dislocation pile ups accumulating at grain boundaries prior to traversing to the next adjacent grain, as opposed to the behaviour in the 45° LPBF specimens where the angle of the grains are more aligned to shear, leading to extended shear paths and a reduction in fatigue strength.

Figs. 8 and 9 display the monotonic and stabilised strain-stress responses of the LPBF 90° and 45° specimens tested under the same conditions (R = −1, ε_{MAX} = 0.6%). In all cases, the materials exhibit a significant degree of plastic deformation given the applied ε_{MAX} values. The monotonic behaviour of the 90° specimens (Fig. 8a) illustrates that the majority of specimens exhibit a period of strain hardening after the material yields, and again shows the reduced performance seen in the as-built finish as compared to the other surface conditions. A similar behaviour is seen in Fig. 9a for the 45° angled specimens, but the extent of strain hardening is far lower. Of greater note here is the variation seen in the yield strengths of the respective variants in material finishes. Whereas the yield strength of the 45° as-built then 150 µm Rösler polish specimen is 390 MPa, the as-built finish with no further conditioning exhibits approximately half this value, with the yield strengths of the other variants ranging between these two extremes. This range is far higher than that seen in the 90° specimens, where yield strength was found to vary by approximately 50 MPa. The reason for the greater variation in the 45° specimens can be related to the layer-by-layer manufacturing process, the greater role of partially melted powder particles on the surface and the 'stepped' nature of the as-built surface finish. This will inherently induce a rougher finish on the material and this is reflected in Table 5, where the vast majority of the roughness parameters are higher in the as-built 45° specimens as compared to the 90° equivalents. Therefore, given the greater depth of material affected by the as-built surface roughness, it is likely that the 45° as-built specimen had a reduced load bearing cross section, and subsequently, a lower yield strength when compared to specimens where the surface is more consolidated and uniform. Cross-comparing the two build

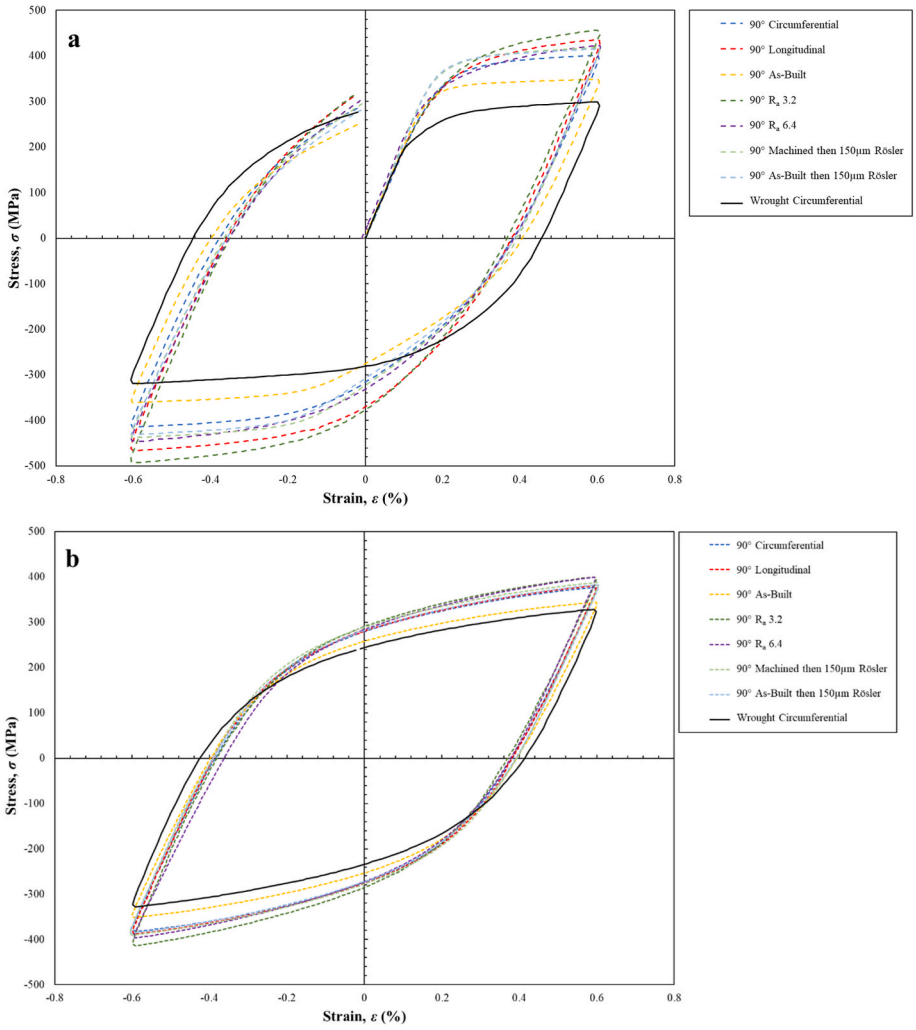

Fig. 8. a) Monotonic and b) Stabilised strain-stress loop behaviour for LPBF 90° specimens compared to wrought equivalent, each tested at $\varepsilon_{MAX} = 0.6\%$.

orientations under the most optimal surface condition, namely the machined then 150 µm polish, the 45° material offers a superior yield strength (350 MPa as compared to 305 MPa), yet stress relaxes to a lesser extent when considering their respective stabilised behaviours. Whereas both material variants experience similar degrees of cyclic softening, the σ_{MAX} of the 90° machined then 150 µm polished sample drops from approximately 450 MPa in the monotonic cycle to around 375 MPa at the half life condition, whilst the 45° equivalent falls from a σ_{MAX} of 450 MPa on the first cycle to 400 MPa in the stabilised condition.

It is commonly acknowledged that fatigue crack initiation in ductile alloys, like SS316LN, is predominantly attributed to the occurrence of localised deformation in persistent slip bands (PSB), whose presence is related to the orientation of the surface grains. This of course is linked to the manufacturing build orientation, where 45° angled specimens would have more favourably orientated grains and high angle grain boundaries, which promote dislocation build up and inhibit an accelerated rate of crack growth. This is linked to the very early stages of initiation and propagation of microstructurally short cracks (MSC), with lengths in the order of only a few grains that are mainly governed by the material microstructure. Additional factors such as surface roughness, grain or phase boundaries and inclusions also contribute to the cause of MSC nucleation. In a highly polished specimen, the local mechanisms responsible for MSC initiation and micro-propagation are restricted to PSBs or elastic anisotropy and plastic incompatibilities at boundaries. Therefore, they are defined at the microscale and are closely related to grain orientation. Grain orientation also plays a role in the crack propagation behaviour of a specimen with an as-built surface condition. However, in these samples, it is likely that stage I fatigue is bypassed and the fatigue mechanism starts in the stage II regime, leading to a reduction in the overall fatigue life.

In comparison, the LCF behaviour in the wrought material is vastly inferior, despite the strong presence of twin boundaries. Heinz et al. [28] evaluated the effects of twin boundaries in austenitic stainless steel through the use of anisotropic elastic models and deduced that the presence of twins induced local stress concentration. In the case of twin laminae with large Schmid factor values, the stress concentration enables and enhances the migration of dislocations along or parallel to the slip plane and promotes strain localisation, which subsequently increases the likelihood of nucleating a fatigue crack at a twin location, thus reducing the material's cyclic performance.

3.3. Surface roughness

In order to isolate the effects of surface finish on fatigue performance, irrespective of the underlying microstructure that differs due to epitaxial grain growth and the role this plays in dictating fatigue resistance, each of the surface parameters were compared against the average fatigue life for specimens from the various data sets that were subjected to the same testing conditions ($\varepsilon_{MAX} = 0.6\%$). The results are presented in Table 5 and reveal that a highly contrasting behaviour exists between fatigue life and the various surface roughness parameters when considering the generated R^2 value that is produced from a power

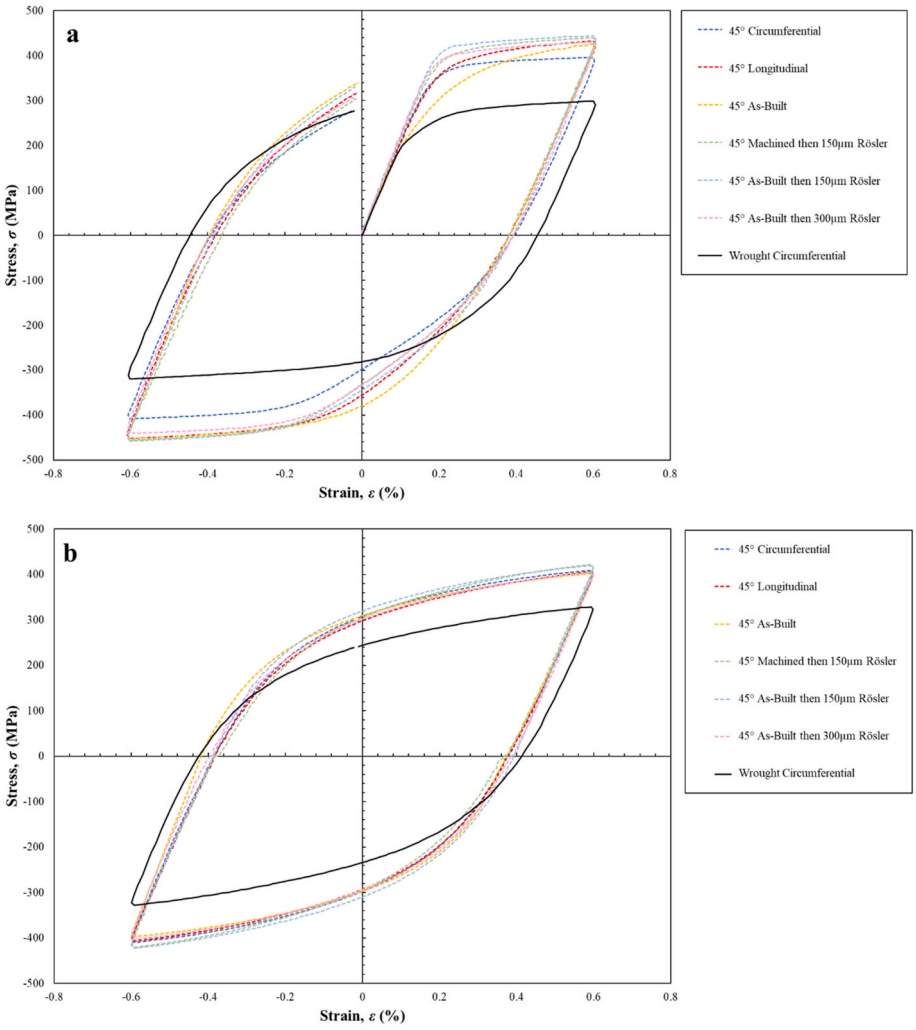

Fig. 9. a) Monotonic and b) Stabilised strain-stress loop behaviour for LPBF 45° specimens compared to wrought equivalent, each tested at $\varepsilon_{MAX} = 0.6\%$.

trendline when fatigue life is plotted against each respective parameter. Whereas the parameters R_{ku}, R_{dq}, R_{pk}, R_{mr1}, R_{mr2}, S_{mr1}, S_{mr2} offer a poor correlation ($R^2 < 0.1$) and therefore no dependency on LCF life, it appears that the strongest relationship is found in S_a, S_q, R_c and S_k ($R^2 =$ 0.45, 0.45, 0.44 and 0.42 respectively). However given that the most optimal R^2 value achieved is 0.45, this clearly determines that surface roughness can not be considered as the single controlling mechanism that influences fatigue performance, and that the underlying material microstructure also has a role.

Visual representations of a selection of the different surface finishes are displayed in Fig. 4. As would be expected, the longitudinally polished specimens have a similar appearance irrespective of material type. However, the appearance of the as-built specimens in the different build orientations differs. AM parts in the as-built surface condition typically have a significantly higher surface roughness relative to their traditionally-manufactured counterparts as a result of the repetitive build-up of material from powder feedstock. Previously, Frazier [29] attributed the surface roughness of AM components to a number of factors, including the AM process type, the process parameters, powder size, geometry, build layer thickness and most critically in this research, build orientation. As seen in Table 5, there is a distinct difference in the surface morphology when a component is built in a vertical orientation than in a diagonal orientation.

The first thing to consider here is the interaction between the melt pool, consolidated material and surrounding powder bed. Fig. 10 shows three different melt pool scenarios for horizontal upskin, vertical wall and 45° downskin surfaces. For the horizontal upskin, the melt pool is fully surrounded either by previously consolidated material or powder about to be melted. This results in a comparatively smooth surface finish with negligible loose powder partially bonding to the surface during cooling. For the vertical wall, half of the melt pool is exposed to unmelted powder that is not subsequently melted. This loose powder in contact with the melt pool only partially melts and results in multiple powder particles adhering to the surface, increasing the surface roughness. For the downskin 45° surface, the majority of the melt pool is exposed to loose powder, along with the base of the melt pool not being supported by consolidated material. This enables the melt pool to sink into the loose powder bed below, increasing in size and partially melting a large number of powder particles. This results in surface breaking features greater than the size of a single powder particle or layer thickness and a significantly higher surface roughness.

In addition to this a second phenomena, staircasing, occurs during AM whereby the layer-by-layer nature of the AM process produces a staircasing on the outer surface of the component that leads to a high surface roughness, particularly on curved or inclined surfaces, as is the case for the 45° angled builds. The staircasing effect is essentially controlled by the layer thickness of the process, where each step is linked to the dimension of each melt layer.

Whilst optimisation of parameters and powder can help to reduce these effects, it is always likely that a component built at an angle will exhibit more severe staircasing and partially melted powder particles, as opposed to a sample built in a vertical orientation, which will in turn

Table 5
Surface roughness parameters for LPBF SS316LN specimens tested under LCF conditions, $\varepsilon_{MAX} = 0.6\%$. R^2 values refer to the goodness of fit from power trendlines for each roughness parameter (Long. = longitudinally polished, Circum. = circumferential, AB = as-built, Mach. 150/300 μm Ros. = Machined then 150/300 μm Rösler polish).

	90° Circum.	90° Long.	90° AB	90° R_a 3.2	90° R_a 6.4	90° Mach. 150 μm Ros.	90° AB 150 μm Ros.	45° Circum.	45° Long.	45° AB	45° Mach. 150 μm Ros.	45° AB 150 μm Ros.	45 AB 300 μm Ros.	R^2 Value
N_f	2512	7093	2401	2160	1745	2875	2491	2470	3766	1383	1831	1545	2893	
R_a (μm)	0.22	0.20	14.42	3.82	7.61	0.29	0.42	0.51	0.21	22.06	0.36	0.19	0.16	0.3621
R_q (μm)	0.27	0.25	17.02	4.54	8.84	0.37	0.55	0.61	0.27	26.91	0.45	0.22	0.20	0.3662
R_t (μm)	1.60	1.26	74.27	17.27	31.08	1.45	2.75	2.67	1.30	128.34	2.37	1.10	1.19	0.3662
R_z (μm)	1.18	0.90	39.37	11.22	19.61	1.16	1.44	1.87	0.91	83.65	1.16	0.74	0.71	0.3955
R_{MAX} (μm)	1.46	1.18	74.27	14.23	28.37	1.60	2.24	2.41	1.18	122.29	1.54	1.10	1.11	0.349
R_p (μm)	0.80	0.62	40.71	9.11	18.75	1.00	1.38	1.42	0.89	57.68	0.98	0.64	0.42	0.3316
R_v (μm)	0.76	0.65	33.57	8.16	12.33	0.95	1.37	1.25	0.46	70.66	1.40	0.45	0.78	0.3867
R_c (μm)	0.83	0.65	40.94	13.46	29.36	1.07	1.64	1.44	0.76	94.70	0.80	0.61	0.58	0.4398
R_{sm} (μm)	38.33	60.05	109.23	208.96	290.62	129.07	197.82	73.76	75.20	219.69	128.21	82.16	85.43	0.2923
R_{ku}(μm)	2.85	2.70	2.47	2.15	2.14	3.19	4.52	2.18	3.46	2.84	3.82	2.69	5.38	0.0025
R_{dq} (μm)	0.07	0.04	2.71	0.17	0.28	0.04	0.04	0.10	0.04	2.69	0.04	0.04	0.03	0.1783
R_k (μm)	0.65	0.60	23.37	10.67	15.38	0.81	1.09	1.31	0.63	68.45	1.03	0.53	0.50	0.4483
R_{pk} (μm)	0.24	0.21	27.85	4.22	14.32	0.42	0.70	0.74	0.35	14.70	0.27	0.20	0.14	0.1121
R_{vk} (μm)	0.27	0.45	14.43	2.69	1.27	0.38	0.75	0.23	0.15	20.90	0.65	0.16	0.35	0.2468
R_{mr1} (%)	11.22	5.50	35.73	16.62	31.03	12.77	8.19	13.59	14.60	11.89	9.01	7.31	8.37	0.0434
R_{mr2} (%)	87.60	85.75	90.22	89.45	96.76	86.76	85.46	91.70	95.27	88.08	84.36	88.29	90.79	0.0057
S_a (μm)	0.35	0.29	14.16	3.39	6.98	0.43	0.36	0.31	0.30	61.55	0.47	0.19	0.21	0.4516
S_q (μm)	0.44	0.36	17.49	4.11	8.22	0.53	0.53	0.39	0.38	79.80	0.59	0.24	0.28	0.4497
S_p (μm)	2.85	2.10	73.37	14.98	22.55	2.86	2.59	2.60	2.10	96.01	2.89	1.17	2.14	0.266
S_v (μm)	1.90	1.50	42.07	8.80	12.55	1.86	10.29	1.79	1.65	254.46	2.30	1.06	3.07	0.4002
S_z (μm)	4.80	3.59	115.44	23.78	35.10	4.72	12.88	4.39	3.75	350.48	5.19	2.23	5.21	0.3734
S_k (μm)	1.23	0.94	42.47	10.40	15.60	1.39	1.06	0.99	0.99	145.86	1.50	0.64	0.64	0.4208
S_{pk} (μm)	0.46	0.37	24.46	4.34	12.84	0.56	0.47	0.46	0.40	34.37	0.63	0.22	0.32	0.3322
S_{vk} (μm)	0.38	0.32	6.71	1.76	1.13	0.39	0.82	0.33	0.32	76.78	0.57	0.22	0.31	0.4052
S_{mr1} (%)	10.20	10.05	14.73	16.44	27.70	11.71	9.12	10.74	10.34	6.25	10.40	8.99	9.93	0.0225
S_{mr2} (%)	91.00	90.90	96.11	94.12	98.03	91.77	88.34	90.96	91.53	86.94	90.79	90.54	89.23	0.0007
Effective K_t	1.04	1.04	4.75	1.81	2.66	1.05	1.11	1.10	1.04	5.67	1.10	1.04	1.04	

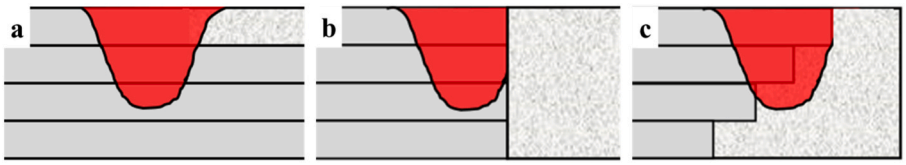

Fig. 10. Schematic of melt pool interactions with an as-built surface for LPBF a) horizontal upskin, b) vertical wall, c) 45° downskin.

also lead to a greater variation in the resulting fatigue life. This is evidenced when considering the standard deviation values generated when analysing the two data sets for the different build orientations. In terms of the parameters that have been found to be most strongly linked to the fatigue life, the as-built 90° specimen exhibited roughness parameters of $S_a = 14.158$, $S_q = 17.493$ $R_c = 40.944$ and $S_k = 42.474$ (and an average respective fatigue life of 2401 cycles, with a standard deviation of 196), as opposed to the 45° equivalent which was $S_a = 61.554$, $S_q = 79.802$, $R_c = 94.704$ and $S_k = 145.855$ (with an average fatigue life of 1383 and a greater standard deviation of 416).

Irrespective of build orientation and the resulting microstructures produced, Fatemi et al. [30] found that fatigue cracks in an AM component with an as-built surface condition will almost always initiate from the surface. Therefore, removal of the rough outer layer thickness by machining or other methods can play a significant role in improving fatigue performance of AM parts. However, it is important to note that one of the key advantages of the AM technique is the capability of fabricating complex geometries as net shape, plus machining of highly intricate and complex geometries can be difficult, if not impossible. Therefore, choosing appropriate powder characteristics and optimising the AM process and design parameters to obtain a smoother surface are important considerations to enhance the fatigue performance.

Pegues et al. [31] undertook a study to assess the role of an as-built surface finish on the fatigue properties of LPBF Ti–6Al–4V, and were able to derive effective stress concentration factors, K_t, from surface roughness information, according to the following relationship:

$$K_t = 1 + n\left(\frac{R_a}{\rho_{10}}\right)\left(\frac{R_t}{R_z}\right) \quad (2)$$

where ρ_{10} refers to the 10-point valley radii, which is estimated as the average radius of the surface breaking pit. For this value, this can be related to the powder size distribution of the SS316LN powder used in this research, which as displayed in Table 2, produced an average diameter of approximately 29 μm (or a radius of 14.5 μm). Using this value for ρ_{10}, the effective values for K_t were calculated and are given in the final row of Table 5. As can be seen, the values produced show good agreement to what would be expected for the different surface finishes. The variants offering the most optimal finishes (longitudinal, circumferential and the samples subjected to the mass finishing procedures) exhibit an effective K_t value of 1.04–1.1, or essentially a surface free from any discontinuities - typical for a highly polished surface finish. However, the as-built surfaces and those that have been deliberately machined to a particular R_a value have a far higher stress concentration factor, with the highest effective K_t found in the as-built 45° sample on the downskin ($K_t = 5.67$). This result is not surprising, given the previous discussion surrounding the staircasing effect, component

orientation and the rough nature of the surface finish on the downskin of an angled build. These calculations corroborate with the images displayed in Figs. 11 and 12, which depict sectioned views of the different surface finish types for both the 90° (Fig. 11) and 45° (Fig. 12) specimens. As can be seen, irrespective of build orientation, the surface finishes for the longitudinal, circumferential and mass finished samples are predominantly flat, with little to no evidence of any surface irregularities or potential areas of stress concentration, whereas the samples remaining in the as-built condition or subjected to deliberate R_a machining exhibit a far rougher surface and a corresponding debit in fatigue performance. This indicates that despite the mass finishing procedures being a less time consuming, labour intensive and costly finishing process compared to the ASTM recommended longitudinal finish, the resulting surface finish is highly comparable, with an effective K_t factor difference of only 0.7 in the 90° specimens, and 0.6 in the 45° samples.

In addition to the calculated K_t values, an effective K_f value can also be derived. K_f refers to the effective fatigue notch factor and be calculated via the following equation:

$$K_f = \frac{Fatigue\ strength\ without\ notch}{Fatigue\ strength\ with\ notch} \tag{3}$$

The K_f factor is typically determined experimentally and originally found application relating to stresses associated with the endurance or fatigue limit of a given material. Subsequently, it has been used throughout the fatigue curve at specified cyclic lives. Given the data available, a fatigue life reference point of approximately 19,000–22,000 cycles has been chosen for the 90° variants, and an N_f of 18,000–19,000 for the 45° specimens, given most of the datasets are available at these points. Based on these assumptions, it appears that the K_f value for the 90° specimens is approximately 358/295 = 1.21, and the equivalent value for the 45° material is approximately 359/328 = 1.09. Using these values, q, the notch sensitivity, can then be calculated as:

$$q = \frac{K_f - 1}{K_t - 1} \tag{4}$$

The value for q typically ranges from 0 (no reduction in fatigue performance) to 1 (maximum effect of the notch, consistent with the elastic stress concentration factor (i.e. $K_f = K_t$)). For the 90° specimens, q was calculated to be 0.056, and for the 45° material, q is derived to be 0.045. These values indicate that despite the alternative surface finish types inducing a variety of stress concentration factors (ranging from 1.04 to 4.75 for the 90° builds, and from 1.04 to 5.67 for the 45° builds), the fatigue performance of the specimens show relatively little sensitivity to the presence of a surface with a high K_t factor, and minimal reduction in cyclic response.

Another important factor to consider when comparing the mechanical response of alternative machined surfaces is the development of residual stresses near or at the surface of the gauge section. A fatigue crack usually nucleates due to the tensile component of stress at the surface of the material being too high. As such, it is often beneficial to impart compressive stress near to or at the surface to oppose any tensile stress to which the component may be subjected to in service. Surface finishing methods, such as invasive techniques including longitudinal and mass finishing procedures, can be employed to change the surface attributes such as the development of compressive stress and produce more uniform surface profiles. Such features can contribute to improving the resistance to wear and cyclic deformation and enhance the load-bearing capability of the material. For this reason the sample preparation guidance in ASTM-E606 [19] specifies gradually reducing cut depths, finishing with a longitudinal polish to minimise tensile stresses at the surface. Hatami et al. [32] performed a series of x-ray diffraction (XRD) analyses to measure the residual stresses in LPBF SS316L. In their study, residual stress profiles were compiled by measuring the stress at several depths below the surface of as-built and longitudinally polished specimens, in order to understand how residual stress behaviour can influence the material's fatigue performance. The authors found that the as-built specimens exhibited high tensile residual stresses both at the surface and up to ~120–140 μm below the surface (approximately 300 MPa). A series of specimens also received post build machining and finishing via longitudinal polishing which helped induce compressive stress in the feed direction [33], situated along the

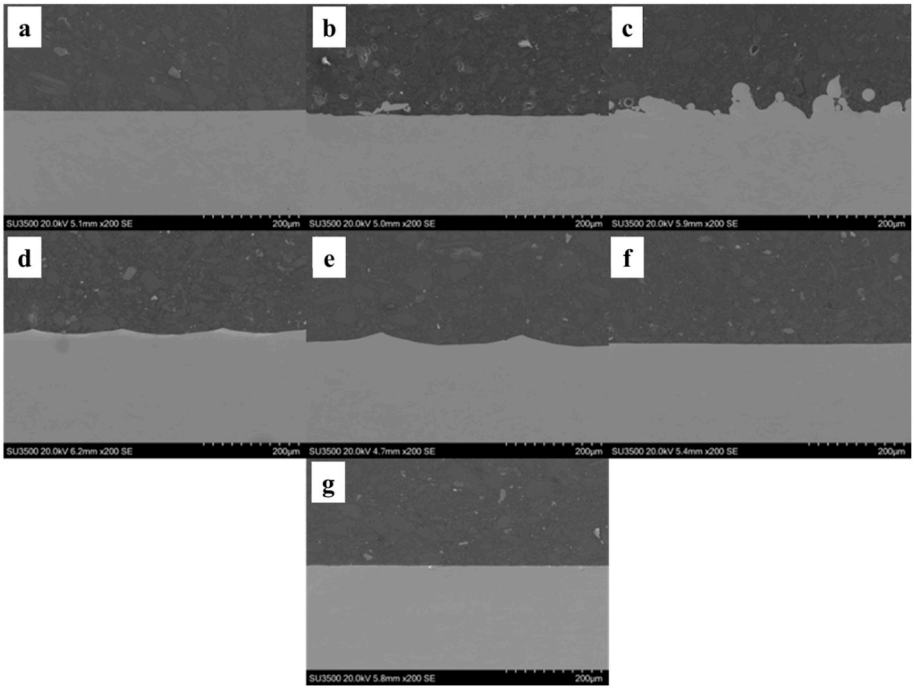

Fig. 11. SEM gauge section images of SS316LN specimens a) LPBF 90°, circumferentially ground, b) LPBF 90°, longitudinal polish, c) LPBF 90°, as-built, d) LPBF 90°, deliberately machined R_a = 3.2 μm, e) LPBF 90°, deliberately machined R_a = 6.4 μm, f) LPBF 90°, machined then Rösler polished with 150 μm removal, g) LPBF 90°, as-built then Rösler polished with 150 μm removal.

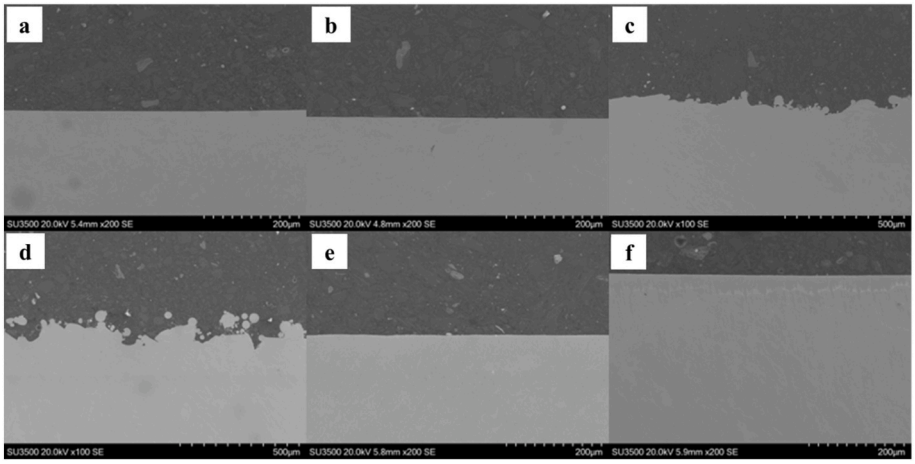

Fig. 12. SEM gauge section images of SS316LN specimens a) LPBF 45°, circumferentially ground, b) LPBF 45°, longitudinal polish, c) LPBF 45°, as-built upskin surface, d) LPBF 45°, as-built downskin surface, e) LPBF 45°, machined then Rösler polished with 150 μm removal, g) LPBF 45°, as-built then Rösler polished with 150 μm removal.

longitudinal axis of the test specimens. The compressive residual stresses were found to be in the order of approximately 200 MPa, and were maintained up to 50–90 μm below the surface. This process had a favourable impact on HCF performance, where at 5×10^5 cycles, the fatigue strength of postmachined specimens was more than 50 MPa higher than the as-built specimens [32]. However, one of the main limitations of longitudinal polishing is that it is not always practical for widespread use on actual component surfaces which typically exhibit complex geometries and inaccessible surfaces. As such, mass finishing is seen as a potential alternative.

Studies on the residual stress behaviour of LPBF as-built surfaces subjected to vibratory mass finishing using Rösler abrasive media have yet to be made available in the public domain. However, some high energy surface treatment methods such as media blasting have been reported, and are used to deliberately impart a compressive residual surface stress that will improve the LCF performance. Peng et al. [34] applied abrasive flow machining (AFM) to improve the as-built surface finish of additively manufactured aluminium alloy AlSi10Mg. The abrasive media employed contained hybrid SiC sizes of 20# and 80# with a mass fraction of 45% and a pressure of 2 MPa. The authors found that the surface roughness was significantly improved after the AFM process, reducing the as-built S_a value from 13 to 14 μm–1.8 μm. Furthermore, a compressive residual stress value of -30.5 ± 7.3 MPa was induced in the surface layer after AFM polishing process, which is significantly lower than the longitudinal polish as reported by Hatami et al. [32]. In comparison, the vibratory mass finishing polishing process investigated in this work is a much lower energy process than media blasting and is therefore considered to induce a negligible level of residual surface stress. Similarly the other surface preparation methods trialled in this study are also low energy and also thought to have minimal effect on residual stress, though this has not been quantified in this study. The fatigue testing completed in this research was performed on samples in their final surface condition and therefore the generated results are thought to be representative of use on a component application.

3.4. Fractography

Post test fractographic studies were conducted on each of the tested specimens in order to evaluate whether any macroscopic and microscopic features influenced the failure mechanisms in the different build orientation and surface finish variants. In each case, the failure process of all the samples resembles a typical crack initiation, propagation and tensile overload stages. Throughout, crack initiation was seen to occur at the surface, with no specimens exhibiting a sub-surface origin for fatigue. This corroborates with the process parameters chosen for the manufacture of the specimens, where the energy density has previously been found to induce an almost fully dense structure (99.95–99.99%) and therefore, little evidence of any process induced defects observed on the fracture faces. Indicative examples of a selection of the fracture surfaces are displayed in Fig. 13, consisting of the longitudinally polished and as-built equivalents for the two LPBF build variants, each of which were tested at room temperature, $R = -1$ and $\varepsilon_{MAX} = 0.6\%$.

Typically, metallic AM specimens that have been machined and/or polished post-manufacture usually exhibit a superior fatigue behaviour relative to their as-built counterparts with rough surfaces [15]. However, whilst the improvement in fatigue behaviour can be envisaged to be directly attributed to an enhanced surface finish, this may not be as significant as that observed for conventional metals if defects such as LoF voids and pores remain after machining the surface, similar to that observed for castings.

Wycisk et al. [35] stated that different crack initiation mechanisms were observed in as-built and machined specimens. In their work on LPBF Ti–6Al–4V, cracks in as-built specimens were observed to almost always initiate from surface, whereas in machined specimens, cracks were predominantly found to initiate from either a surface breaking discontinuity or internal defects. As a result, they found more scatter was present in the fatigue data of the machined specimens, particularly near the endurance limit. Following on from this, Pegues et al. [36] found that fatigue specimens with rough, as-built surfaces, typically have multiple crack initiation sites on the surface. These multiple cracks will start to grow independently until they reach a critical measure and begin to coalesce, leading to the onset of failure. As previously discussed, this can lead to stage II fatigue being activated without the stage I regime, while specimens with machined surfaces mostly have cracks initiating from a single defective feature, such as a lack of fusion or an entrapped gas pore, if present. Such interaction between independently propagating cracks is the main contributor towards a reduced fatigue resistance in material with an as-built finish.

However, the material tested in this research appeared to be fully dense owing to the optimal process parameters that were used resulting in a favourable influence on limiting the presence of process-induced defects. This was thought to increase the sensitivity of fatigue properties to surface breaking defects. At strain amplitudes tested above 0.4% the results show a level of variation in fatigue properties between surface conditions of the SS316LN LPBF specimens larger than the observed scatter, but for strain amplitudes <0.3% this trend is more limited relative to the increased level of scatter. However, it is important to

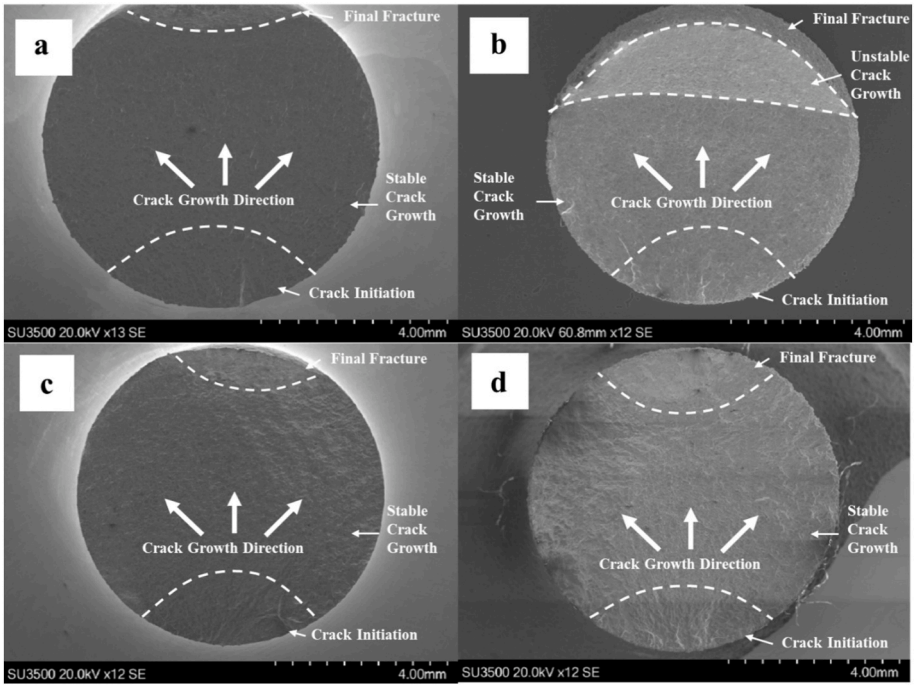

Fig. 13. SEM fracture surface images of SS316LN LPBF LCF specimens tested at $\varepsilon_{MAX} = 0.6\%$, a) LPBF 90°, longitudinal polish, b) LPBF 90°, as-built, c) LPBF 45°, longitudinal polish, d) LPBF 45°, as-built.

consider that five of the seven finishes applied to the 90° LPBF builds were calculated to have an effective K_t value < 1.81, whilst five of the six finishes on the 45° samples exhibited similar values (K_t = <1.10). Therefore, given that a K_t ~1 suggests that a finish is flawless and without any discontinuities, these values have heavily influenced the resulting q factor, dampening the effect of the most severe K_t factor found in the as-built variants in either orientation. As such, further surface finish types, or indeed more severe notch geometries, need to be considered when contemplating the full notch sensitivity of the material.

3.5. Material lifing

The strain based Coffin-Manson approach was employed in this study to obtain fatigue curves and lives that lie outside the results generated in this research and extend into longer fatigue life regimes typically associated with high cycle fatigue (HCF). To obtain these curves the stabilised hysteresis strain-stress loops for all specimens were analysed to determine the cyclic deformation properties of the LPBF 90° and LPBF 45° SS316LN material. Initially the elastic strain amplitude was calculated using the following relationship:

$$\frac{\Delta\varepsilon_e}{2} = \frac{\sigma_a}{E} \tag{5}$$

where $\frac{\Delta\varepsilon_e}{2}$ is the elastic strain amplitude, σ_a is the stress amplitude and E is the Young's modulus. The plastic strain amplitude $\frac{\Delta\varepsilon_p}{2}$ is determined by subtracting the elastic strain amplitude, $\frac{\Delta\varepsilon_e}{2}$ from the total stain, ε_a according to:

$$\frac{\Delta\varepsilon_p}{2} = \varepsilon_a - \frac{\Delta\varepsilon_e}{2} \tag{6}$$

The elastic, $\frac{\Delta\varepsilon_e}{2}$ and plastic $\frac{\Delta\varepsilon_p}{2}$ strain components and the associated number of reversals to failure, $2N_f$, were used to determine the fatigue properties of the LPBF SS316LN variants, using the following equations:

$$\frac{\Delta\varepsilon_e}{2} = \frac{\sigma_f'}{E}(2N_f)^b \tag{7}$$

$$\frac{\Delta\varepsilon_p}{2} = \varepsilon_f'(2N_f)^c \tag{8}$$

Where σ_f' is the fatigue strength coefficient, b is the fatigue strength exponent, ε_f' is the fatigue ductility coefficient, and c is the fatigue ductility exponent. These fatigue properties were determined by applying a linear least square fits to elastic and plastic strain amplitudes versus reversals to failure, whereby the intercept at $2N_f = 1$ for the elastic, $\frac{\Delta\varepsilon_e}{2}$ and plastic $\frac{\Delta\varepsilon_p}{2}$ strain components are b and c respectively. Similarly, the gradient of the elastic, $\frac{\Delta\varepsilon_e}{2}$ and plastic $\frac{\Delta\varepsilon_p}{2}$ strain components against reversals is equal to the fatigue strength coefficient, σ_f' and the fatigue strength exponent, ε_f' respectively. Overall this provides the total strain amplitude versus fatigue life data given by the equation below:

$$\frac{\Delta\varepsilon}{2} = \varepsilon_a = \frac{\Delta\varepsilon_e}{2} + \frac{\Delta\varepsilon_p}{2} = \frac{\sigma_f'}{E}(2N_f)^b + \varepsilon_f'(2N_f)^c \tag{9}$$

The total ε_a-N_f curves were obtained using equations (7)–(9) with selected examples for the as-built and longitudinally polished specimens presented in Figs. 14 and 15 for each build orientation. Figs. 14 and 15 show that irrespective of the two surface finishes demonstrated in both the 90° and 45° orientation, the fatigue behaviour of L-PBF SS316LN is mainly dominated by elastic deformation up to a strain amplitude of approximately 0.0018. This was also the case for the other surface finish types, across both build orientations. However, as would be expected, at higher strain amplitudes (i.e. 0.003 and 0.004), fatigue behaviour is governed by both elastic and plastic deformations.

To understand the effect of surface finish on the fatigue behaviour of the LPBF SS316LN material, the strain amplitude versus reversals to failure data and the Coffin-Manson curves have been plotted in Figs. 16 and 17. The results indicate that the Coffin-Manson approach shows good agreement with experimental data, and also provides an important indication of the predicted fatigue lives of the different LPBF variants under HCF conditions. Fig. 16 also includes data from a previous research article [12] and the Coffin-Manson predictions generated in this research can also be seen to correlate well with this additional data set of LPBF SS316L.

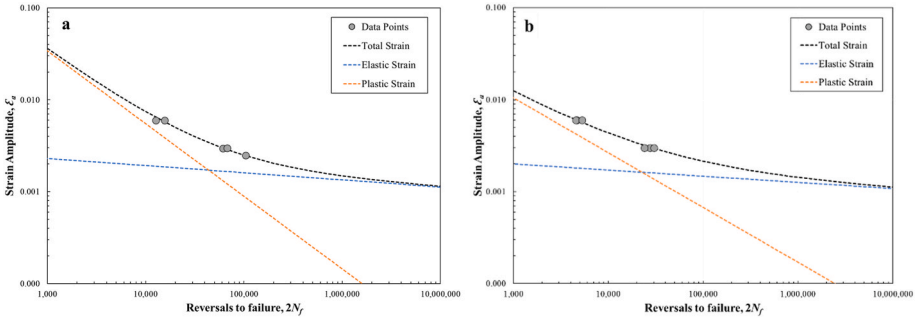

Fig. 14. Elastic, plastic and total ε_a versus reversals to failure response obtained using Coffin-Manson approach for LPBF 90° material with a) longitudinal polish and b) as-built surface finishes.

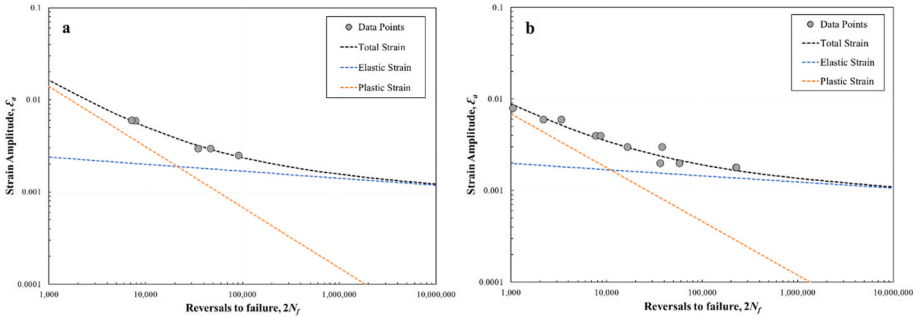

Fig. 15. Elastic, plastic and total ε_a versus reversals to failure response obtained using Coffin-Manson approach for LPBF 45° material with a) longitudinal polish and b) as-built surface finishes.

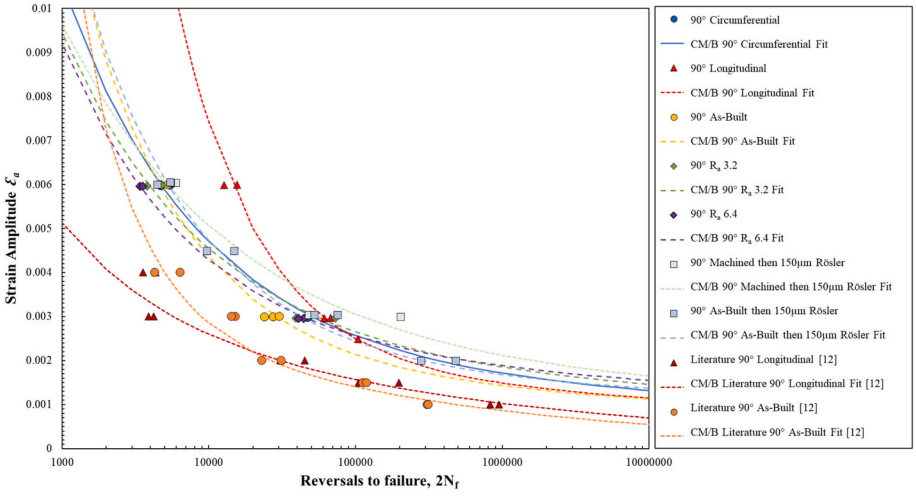

Fig. 16. Coffin-Manson/Basquin fitting curves for LPBF 90° LCF data.

4. Conclusions

In this research, the low cycle fatigue behaviour of laser powder bed fused stainless steel 316LN has been investigated on specimens built in two primary build orientations (90° and 45°) and finished with several alternative polishing procedures. From these results, the following conclusions can be drawn.

- LPBF 90° specimens have been found to have a superior ε-N_f behaviour compared to the diagonally built 45° specimens. However, the 45° build orientation generally offers higher yield strength and cyclically softens less with an increasing number of cycles, resulting in a more superior stabilised σ_a-N_f response. These behaviours are attributed to the directionality of the grains in the two build orientations, where the 90° built specimens have a smaller grain size perpendicular to the build direction, or the face of crack growth, and therefore a shorter slip path as compared to the 45° specimens.
- Surface roughness parameters of S_a, S_q, R_c and S_k show the greatest correlation to fatigue life, but surface roughness can not be considered to be the dominant mechanism controlling fatigue performance.
- Effective K_t values were calculated for all surface finish types and apart from the as-built surface and the machining to a deliberate R_a value, the calculated K_t values fell between 1.04 and 1.11. This encompassed the longitudinally and circumferentially polished samples, in addition to those subjected to the mass finishing

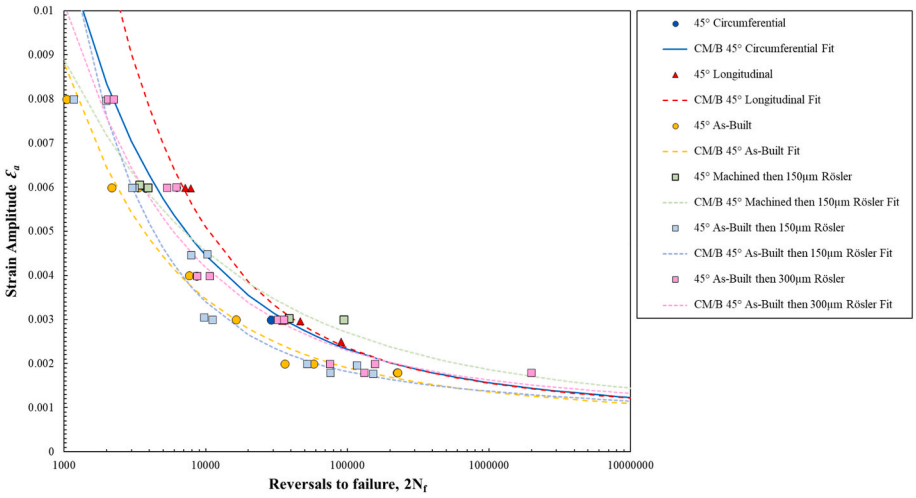

Fig. 17. Coffin-Manson/Basquin fitting curves for LPBF 45° LCF data.

procedures. This narrow range was reflected in the resulting LCF data, where little scatter was seen between the variants exhibiting K_t factors within these values, highlighting that the mass finishing methods provide a time and cost effective alternative of removing the as-built surface and achieving fatigue properties of a similar level to those recommended in international standards.

- The as-built surface of 45° LPBF specimens has a rougher profile compared to the 90° built equivalent. This is due to partially melted powder particles at the surface and the staircasing effect, which are more pronounced in angled builds and lead to a larger effective stress concentration factor at the surface ($K_t = 4.75$ as compared to $K_t = 5.76$ for the 45° specimens).
- Whilst as-built specimens showed a significant reduction in fatigue performance in either vertically or diagonally built specimens, other surface conditions showed a reduced sensitivity at higher strain amplitudes and a minimal reduction in fatigue performance at lower strain amplitudes where scatter in results was seen to increase.
- All fatigue failures initiated from surface locations, highlighting that optimal process parameters were used to produce near fully-dense material with no evidence of process induced defects in the underlying microstructure and resulting fracture faces.
- The Coffin-Manson lifing approach has been found to accurately capture the LCF behaviour of LPBF SS316LN specimens built in alternative build orientations with a variety of surface conditions.

CRediT authorship contribution statement

William Beard: Writing – original draft, Writing – review & editing, Data curation, Investigation, Formal analysis, Visualization. **Robert Lancaster:** Writing – original draft, Writing – review & editing, Conceptualization, Methodology, Supervision, Project administration, Funding acquisition. **Nicholas Barnard:** Data curation, Writing – review & editing, Visualization, Formal analysis. **Thomas Jones:** Data curation, Resources, Supervision, Project administration. **Jack Adams:** Supervision, Project administration.

Declaration of competing interest

The authors declare that they have no known competing financial interests or personal relationships that could have appeared to influence the work reported in this paper.

Data availability

The data that has been used is confidential.

Acknowledgements

The current research was funded by EPSRC Rolls-Royce Strategic Partnership in Structural Metallic Systems for Gas Turbines (grants EP/H500383/1 and EP/H022309/1) alongside The Materials and Manufacturing Academy (M2A) supported through the European Social Fund (grant c80816). The provision of materials and supporting information from Rolls-Royce plc is gratefully acknowledged. Mechanical tests were performed at Swansea Materials Research and Testing Ltd. (SMaRT).

References

[1] S. Ford, M. Despeisse, Additive manufacturing and sustainability: an exploratory study of the advantages and challenges, J. Clean. Prod. 137 (2016), https://doi.org/10.1016/j.jclepro.2016.04.150.
[2] N. Shamsaei, A. Yadollahi, L. Bian, S.M. Thompson, An overview of Direct Laser Deposition for additive manufacturing; Part II: mechanical behavior, process parameter optimization and control, Addit. Manuf. 8 (2015), https://doi.org/10.1016/j.addma.2015.07.002.
[3] R. Shrestha, J. Simsiriwong, N. Shamsaei, S.M. Thompson, L. Bian, Effect of build orientation on the fatigue behavior of stainless steel 316L manufactured via a laser-powder bed fusion process, in: Solid Freeform Fabrication 2016: Proceedings of the 27th Annual International Solid Freeform Fabrication Symposium - an Additive Manufacturing Conference, SFF 2016, 2016.
[4] A.B. Spierings, T.L. Starr, K. Wegener, Fatigue performance of additive manufactured metallic parts, Rapid Prototyp. J. 19 (2) (2013), https://doi.org/10.1108/13552541311302932.
[5] J.J. Lewandowski, M. Seifi, Metal additive manufacturing: a review of mechanical properties, Annu. Rev. Mater. Res. 46 (2016), https://doi.org/10.1146/annurev-matsci-070115-032024.
[6] B. Bhushan, Surface roughness analysis and measurement techniques, in: Modern Tribology Handbook: Volume One: Principles of Tribology, 2000, https://doi.org/10.1201/9780849377877-10.
[7] J.C. Snyder, K.A. Thole, Understanding laser powder bed fusion surface roughness, J. Manuf. Sci. Eng. 142 (7) (Jul. 2020), https://doi.org/10.1115/1.4046504.
[8] C. Qiu, C. Panwisawas, M. Ward, H.C. Basoalto, J.W. Brooks, M.M. Attallah, On the role of melt flow into the surface structure and porosity development during selective laser melting, Acta Mater. 96 (Sep. 2015) 72–79, https://doi.org/10.1016/j.actamat.2015.06.004.
[9] A. Uriondo, M. Esperon-Miguez, S. Perinpanayagam, The present and future of additive manufacturing in the aerospace sector: a review of important aspects, Proc Inst Mech Eng G J Aerosp Eng 229 (11) (2015) 2132–2147, Sep, https://doi.org/10.1177/0954410014568797.
[10] T. DebRoy, et al., Additive manufacturing of metallic components – process, structure and properties, Prog. Mater. Sci. 92 (Mar. 2018) 112–224, https://doi.org/10.1016/j.pmatsci.2017.10.001.
[11] M. Zhang, et al., Fatigue and fracture behaviour of laser powder bed fusion stainless steel 316L: influence of processing parameters, Mater. Sci. Eng. 703 (2017), https://doi.org/10.1016/j.msea.2017.07.071.
[12] R. Shrestha, J. Simsiriwong, N. Shamsaei, Fatigue behavior of additive manufactured 316L stainless steel parts: effects of layer orientation and surface roughness, Addit. Manuf. 28 (2019), https://doi.org/10.1016/j.addma.2019.04.011.

[13] A. Yadollahi, N. Shamsaei, S.M. Thompson, A. Elwany, L. Bian, Effects of building orientation and heat treatment on fatigue behavior of selective laser melted 17-4 PH stainless steel, Int. J. Fatig. 94 (2017), https://doi.org/10.1016/j.ijfatigue.2016.03.014.
[14] T.M. Mower, M.J. Long, Mechanical behavior of additive manufactured, powder-bed laser-fused materials, Mater. Sci. Eng. 651 (2016), https://doi.org/10.1016/j.msea.2015.10.068.
[15] A.B. Spierings, T.L. Starr, K. Wegener, Fatigue performance of additive manufactured metallic parts, Rapid Prototyp. J. 19 (2) (2013), https://doi.org/10.1108/13552541311302932.
[16] A. Leicht, M. Rashidi, U. Klement, E. Hryha, Effect of process parameters on the microstructure, tensile strength and productivity of 316L parts produced by laser powder bed fusion, Mater. Char. 159 (Jan. 2020), 110016, https://doi.org/10.1016/j.matchar.2019.110016.
[17] J.A. Cherry, H.M. Davies, S. Mehmood, N.P. Lavery, S.G.R. Brown, J. Sienz, Investigation into the effect of process parameters on microstructural and physical properties of 316L stainless steel parts by selective laser melting, Int. J. Adv. Manuf. Technol. 76 (5–8) (Feb. 2015) 869–879, https://doi.org/10.1007/s00170-014-6297-2.
[18] H.V. Atkinson, S. Davies, Fundamental aspects of hot isostatic pressing: an overview, Metall. Mater. Trans. 31 (12) (Dec. 2000) 2981–3000, https://doi.org/10.1007/s11661-000-0078-2.
[19] ASTM E 606, Standard Practice for Strain-Controlled Fatigue Testing, Astm, 2010.
[20] Rösler, "Rösler Mass Finishing Brochure.".
[21] ISO 21920-3:2021, Geometrical product specifications (GPS) — surface texture: profile — Part 3: specification operators, ISO (2021).
[22] W.E. Frazier, Metal additive manufacturing: a review, J. Mater. Eng. Perform. 23 (6) (2014) 1917–1928, https://doi.org/10.1007/s11665-014-0958-z.
[23] S. Sinha, J.A. Szpunar, N.A.P. Kiran Kumar, N.P. Gurao, Tensile deformation of 316L austenitic stainless steel using in-situ electron backscatter diffraction and crystal plasticity simulations, Mater. Sci. Eng. 637 (Jun. 2015) 48–55, https://doi.org/10.1016/j.msea.2015.04.005.
[24] Z. Sun, X. Tan, S.B. Tor, C.K. Chua, Simultaneously enhanced strength and ductility for 3D-printed stainless steel 316L by selective laser melting, NPG Asia Mater. 10 (4) (Apr. 2018) 127–136, https://doi.org/10.1038/s41427-018-0018-5.
[25] N.P. Lavery, et al., Effects of hot isostatic pressing on the elastic modulus and tensile properties of 316L parts made by powder bed laser fusion, Mater. Sci. Eng. 693 (March) (2017) 186–213, https://doi.org/10.1016/j.msea.2017.03.100.
[26] S. Afkhami, M. Dabiri, S.H. Alavi, T. Björk, A. Salminen, Fatigue characteristics of steels manufactured by selective laser melting, Int. J. Fatig. 122 (November 2018) (2019) 72–83, https://doi.org/10.1016/j.ijfatigue.2018.12.029.
[27] D. Kong, C. Dong, X. Ni, Z. Liang, C. Man, X. Li, Hetero-deformation-induced stress in additively manufactured 316L stainless steel, Mater. Res. Lett. 8 (10) (Oct. 2020) 390–397, https://doi.org/10.1080/21663831.2020.1775149.
[28] A. Heinz, P. Neumann, Crack initiation during high cycle fatigue of an austenitic steel, Acta Metall. Mater. 38 (10) (Oct. 1990) 1933–1940, https://doi.org/10.1016/0956-7151(90)90305-Z.
[29] W.E. Frazier, Metal additive manufacturing: a review, J. Mater. Eng. Perform. 23 (6) (Jun. 2014) 1917–1928, https://doi.org/10.1007/s11665-014-0958-z.
[30] A. Fatemi, et al., Fatigue behaviour of additive manufactured materials: an overview of some recent experimental studies on <scp>Ti-6Al-4V</scp> considering various processing and loading direction effects, Fatig. Fract. Eng. Mater. Struct. 42 (5) (May 2019) 991–1009, https://doi.org/10.1111/ffe.13000.
[31] J.W. Pegues, N. Shamsaei, M.D. Roach, R.S. Williamson, Fatigue life estimation of additive manufactured parts in the as-built surface condition, Mater Design. Process Commun. 1 (3) (Jun. 2019), https://doi.org/10.1002/mdp2.36.
[32] S. Hatami, T. Ma, T. Vuoristo, J. Bertilsson, O. Lyckfeldt, Fatigue strength of 316 L stainless steel manufactured by selective laser melting, J. Mater. Eng. Perform. 29 (5) (May 2020) 3183–3194, https://doi.org/10.1007/s11665-020-04859-x.
[33] D.Y. Jang, T.R. Watkins, K.J. Kozaczek, C.R. Hubbard, O.B. Cavin, Surface residual stresses in machined austenitic stainless steel, Wear 194 (1–2) (Jun. 1996) 168–173, https://doi.org/10.1016/0043-1648(95)06838-4.
[34] C. Peng, Y. Fu, H. Wei, S. Li, X. Wang, H. Gao, Study on improvement of surface roughness and induced residual stress for additively manufactured metal parts by abrasive flow machining, Procedia CIRP 71 (2018) 386–389, https://doi.org/10.1016/j.procir.2018.05.046.
[35] E. Wycisk, A. Solbach, S. Siddique, D. Herzog, F. Walther, C. Emmelmann, Effects of defects in laser additive manufactured Ti-6Al-4V on fatigue properties, Phys. Procedia 56 (2014) 371–378, https://doi.org/10.1016/j.phpro.2014.08.120.
[36] J. Pegues, M. Roach, R. Scott Williamson, N. Shamsaei, Surface roughness effects on the fatigue strength of additively manufactured Ti-6Al-4V, Int. J. Fatig. 116 (Nov. 2018) 543–552, https://doi.org/10.1016/j.ijfatigue.2018.07.013.